12-2009

Block Modeling with Multiple Fault Network Geometries and a Linear Elastic Coupling Estimator in Spherical Coordinates

Brendan J. Meade
Harvard University

John P. Loveless
Smith College, jloveles@smith.edu

Bulletin of the Seismological Society of America, Vol. 99, No. 6, pp. 3124–3139, December 2009, doi: 10.1785/0120090088

Block Modeling with Connected Fault-Network Geometries and a Linear Elastic Coupling Estimator in Spherical Coordinates

by Brendan J. Meade and John P. Loveless

Abstract Geodetic observations of interseismic deformation provide constraints on the partitioning of fault slip across plate boundary zones, the spatial distribution of both elastic and inelastic strain accumulation, and the nature of the fault system evolution. Here we describe linear block theory, which decomposes surface velocity fields into four components: (1) plate rotations, (2) elastic deformation from faults with kinematically consistent slip rates, (3) elastic deformation from faults with spatially variable coupling, and (4) homogeneous intrablock strain. Elastic deformation rates are computed for each fault segment in a homogeneous elastic half-space using multiple optimal planar Cartesian coordinate systems to minimize areal distortion and triangular dislocation elements to accurately represent complex fault system geometry. Block motions, fault-slip rates, elastic coupling, and internal block strain rates are determined simultaneously using a linear estimator with constraints from both geodetically determined velocity fields and geologic fault-slip rate estimates. We also introduce algorithms for efficiently implementing alternative fault-network geometries to quantify parameter sensitivity to nonlinear perturbations in model geometry.

Introduction

Understanding the partitioning of deformation in the continental crust at plate boundary zones is crucial for assessing the balance between seismic moment release and interseismic strain accumulation, identifying whether or not crustal deformation processes are consistent over geologic and geodetic time scales, and providing the velocity constraints that dynamic models may be tested against. Wide aperture and spatially dense Global Positioning System (GPS) networks provide measurements of nominally interseismic crustal velocities at the Earth's surface averaged over 1–15 yr intervals, with a typical precision of <2 mm/yr, and are the primary source of kinematic data used to constrain plate boundary zone deformation processes. Geodynamic models used to explain these data in actively deforming continental regions can generally be divided into four categories: (1) continuum, (2) microplate, (3) fault/earthquake cycle, and (4) block models. To put our work into context, we review these approaches and consider how each has been applied to contemporary geodetic observations of both geodynamic and earthquake processes.

Continuum descriptions of active plate boundary zones represent surface velocities using either spherical interpolation methods (e.g., Haines and Holt, 1993; Shen-Tu *et al.*, 1999; Holt *et al.*, 2000) or viscous rheologies (e.g., Molnar and Gipson, 1996; Flesch *et al.*, 2000, 2001; England and Molnar, 2005) as effective means of approximating the motions of the possibly large number of lithospheric blocks where an explicit representation of each might be considered impractical (e.g., Molnar, 1988). This work has exploited the thin viscous sheet approximation (England and McKenzie, 1982) as an effective model for the bulk lithosphere. Thin viscous sheet models have provided insight into the relative importance of the forces that drive lithospheric deformation (England and Houseman, 1986, 1989; England and Molnar, 1997) but do not allow for mechanically meaningful interpretations of geodetic velocity fields. In general, continuum models do not explicitly account for earthquake cycle processes including postseismic deformation and interseismic elastic strain accumulation (Liu and Bird [2008] is a notable exception). Moreover, analytic and computational studies of the lithospheric behavior that consider the interactions between a finite thickness elastic upper crust and a viscous (or viscoelastic) lower layer have demonstrated that steady-state surface velocity fields do not provide diagnostic information about the distribution of deformation throughout the viscous layer, which constitutes the bulk of the lithosphere (Savage, 2000; Zatman, 2000; Hetland and Hager, 2004).

Microplate models also do not consider earthquake cycle effects but are predicated on the assumption that geodetically observed velocities result from the rotation of a finite number of crustal microplates (e.g., Shen *et al.*, 2005; Thatcher, 2007). In other words, these models are a direct application of plate tectonic theory to continental tectonics. This class of models explicitly includes localized fault zones

and predicts discrete velocity discontinuities across these zones. While geological slip rate estimates are based on the observation of displacements across localized structures, discrete velocity discontinuities across fault zones are rarely seen in geodetic observations of interseismic deformation. Instead, geodetic velocities across active faults are generally characterized by gradual velocity gradients (e.g., Savage and Burford, 1973), and thus microplate models are often constrained only by GPS data away from faults where it is assumed that earthquake cycle processes are negligible (e.g., Thatcher, 2007).

In contrast, models of fault and earthquake cycle processes typically assume that geodetically observed velocity fields result from the elastic behavior of the upper crust and viscoelastic behavior of the lower crust/upper mantle. The mechanical concept underlying these models is that, during the interseismic part of the seismic cycle, either localized slip (Savage and Burford, 1973) or viscoelastic relaxation (Nur and Mavko, 1974; Savage and Prescott, 1978; Savage, 2000) below the seismogenic layer exert a stress on the elastic upper crust and causes it to deform. In general, viscoelastic earthquake cycle models predict time-dependent surface motions. However, in the limiting case where the ratio of the earthquake repeat interval to the Maxwell time (dynamic viscosity divided by shear modulus) is <1, fault parallel velocity profiles deviate negligibly from the steady-state expectation (e.g., Savage and Prescott, 1978; Savage, 2000; Hilley *et al.*, 2005). Earthquake cycle models have been used to explain geodetic observations in continental settings such as the San Andreas fault (Savage and Burford, 1973; Feigl *et al.*, 1993), the Himalayan Range Front, and southern Tibet (Bilham *et al.*, 1997; Jouanne *et al.*, 2004; Feldl and Bilham, 2006), as well as mixed continental–oceanic settings found at subduction zones including Cascadia (Savage, 1983; Flück *et al.*, 1997; Wang *et al.*, 2003) and Japan (Le Pichon *et al.*, 1998; Mazzotti *et al.*, 2000). This class of models has also been widely used to make comparisons with geologically estimated fault-slip rates (e.g., Segall, 2002), image the geometry of active faults (e.g., Harris and Segall, 1987), and assess the spatial distribution of fault coupling (e.g., Bürgmann *et al.*, 2005).

The effects of both earthquake cycle processes and block (or microplate) motions are combined in block models. In these models, motion due to multiple rotating blocks is supplemented by elastic deformation due to fault slip at block boundaries without the *a priori* assumption that one effect or the other dominates the observed velocity field. Early block models (Matsu'ura *et al.*, 1986; Hashimoto and Jackson, 1993) estimated block motions and fault-slip rates independently and were kinematically inconsistent in the sense that the fault-slip rates contributing to elastic deformation were not a function of block motions or were permitted to be strike slip only (Bennett *et al.*, 1996, 1997). Souter (1998) allowed fault-slip rates to be defined by differential block motion at the faults defining block boundaries, implicitly satisfying the path integral velocity constraint (e.g., Minster and Jordan, 1987) for arbitrarily dipping faults in three dimensions with multiple slip components. While kinematically consistent slip rates predict smooth interseismic velocity transitions from block to block, they fail to allow enough variation in apparent elastic coupling to accurately model the partially coupled behavior of subduction zones (e.g., Savage, 1983; Flück *et al.*, 1997; Genrich *et al.*, 2000; McCaffrey *et al.*, 2000). McCaffrey (2005) introduced homogeneous internal block strain as a proxy for distributed deformation that provides a means of quantifying deformation associated with unresolved structures.

Here we extend block theory (Matsu'ura *et al.*, 1986; Hashimoto and Jackson, 1993; Souter, 1998; Bennett *et al.*, 1996, 1997; Murray and Segall, 2001; McCaffrey, 2002; Meade and Hager, 2005) using spherical geometry with locally optimal coordinate transformations, triangular dislocation elements (TDEs) for accurately representing three-dimensional fault system geometry, and a linear estimator to simultaneously solve for block motions, kinematically consistent (fully coupled) fault-slip rates, and effective elastic coupling coefficients. A linear solution is advantageous over previously used nonlinear approaches because it allows for an analytic solution given a fault-network configuration, and the calculation of model sensitivities and formally propagated uncertainties is straightforward. We also introduce an unsupervised algorithm for determining the connectivity and relative orientations of the fault and block system based on the fault segment geometry alone, facilitating the analysis of a wide range of geometrically complex models. To demonstrate the decomposition of a geodetically observed velocity field, we use the GeoNet data from Japan and a nationwide block model (Loveless and Meade, 2009).

Linear Block Theory

Block theory is a method for decomposing a geodetically observed velocity field into block motion, elastic, and homogeneous intrablock deformation components. We describe the east, north, and up (ENU) components of the quasistatic nominally interseismic velocity, $\tilde{\mathbf{v}}_I$, recorded at each GPS station (with the geographical longitude, latitude, and height coordinates $\tilde{\mathbf{x}} = [\theta, \phi, R]^{\mathsf{T}}$, where R is the Earth's radius) as the sum of three tectonic processes: (1) block rotation, (2) elastic strain accumulation, and (3) internal block deformation,

$$\tilde{\mathbf{v}}_I = \tilde{\mathbf{v}}_B + \tilde{\mathbf{v}}_E + \tilde{\mathbf{v}}_\epsilon. \tag{1}$$

(See Table A1 for a list of symbols used.) To illustrate how a smooth interseismic velocity field may result from the combined effects of block motion and elastic strain accumulation processes, we develop a simple two block model in flat Cartesian space with vertical faults locked to a depth of 15 km (Fig. 1). The 150×150 km internal block moves northward at 100 mm/yr relative to the fixed external block (Fig. 1a). Differential block motions are 100 mm/yr at each of the four

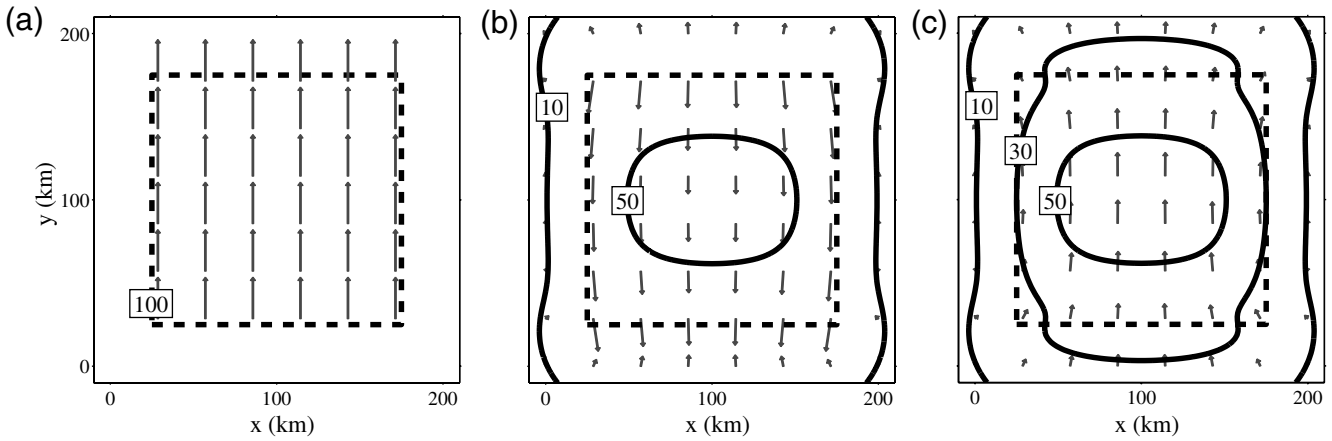

Figure 1. Block motions, elastic, and interseismic deformation in a simple two-block model. (a) The gray velocity vectors show a northward translation of the interior block at 1 mm/yr. The black dashed line shows the four fault segments that define the boundary between the two blocks. Differential block motion at the block boundaries left-lateral, right-lateral, divergent, and convergent fault slip at the west, east, south, and north boundaries, respectively. Tensile dislocations are used to calculate the elastic deformation associated with the divergent and convergent margins. In this simple model, fault-slip rates are given by differential block motions on vertical fault segments extending to 20 km depth; the elastic deformation associated with slip on these structures is shown in (b). (b) The solid black lines show contours of velocity magnitude as a percentage of the northward block motion, with the fastest rates nearest the block boundaries. On the exterior block, the elastic deformation decays to 10% within 15–30 km of the block boundaries, while ~60% of the interior block area exceeds 50% of the block motion signal. (c) Block motion and elastic deformation combine to produce a continuous velocity field typical of interseismic geodetic observations. Here the velocity contours increase monotonically toward the center of the interior block, reaching a maximum of ~70% of the northward block motion.

block boundaries with left-lateral strike slip, right-lateral strike slip, extensional tensile slip (opening mode), and contractional tensile slip (closing mode) at the west, east, south, and north fault segments, respectively. Tensile-slip dislocation sources may serve as approximations to dipping reverse and normal faulting structures (Souter, 1998). This approximation neglects realistic faulting geometry in contractional and extensional environments but has been applied in dominantly strike-slip regimes (Becker *et al.*, 2005; Meade and Hager, 2005; McCaffrey, 2005), as the horizontal deformation produced by a tensile dislocation is somewhat similar to that produced by dipping faults (Fig. 2). Deformation due to interseismic elastic strain accumulation is localized near each segment boundary and cumulatively results in largely southward directed velocities within the interior block that reach ~40% of the magnitude of the block motion (Fig. 1b). In this simple example, the superposition of block motions and elastic strain accumulation produces an interseismic velocity field with smooth velocity gradients near fault segments (Fig. 1c). Here the apparently continuous interseismic velocity field does not result from the motion of a large number of small blocks (i.e., as in continuum theories) but rather the combined effect of both block motions and earthquake cycle processes.

Blocks motions in spherical coordinates can be defined using a Cartesian rotation vector, $\mathbf{\Omega}$, passing through the center of the Earth, as $\hat{\mathbf{v}}_B = \mathbf{\Omega} \times \hat{\mathbf{x}}$, where $\hat{\mathbf{x}} = [\hat{x}, \hat{y}, \hat{z}]^\mathsf{T} = [R\cos\phi\cos\theta, R\cos\phi\sin\theta, R\sin\theta]^\mathsf{T}$ are the Cartesian station coordinates. Both the cross product and the conversion from Cartesian to ENU velocity, $\tilde{\mathbf{v}}_B$, can be written in terms of linear operators (Cox and Hart, 1986) as

$$\tilde{\mathbf{v}}_B = \mathbf{P}_V \mathbf{G}_B \mathbf{\Omega} = \begin{bmatrix} -\sin\phi\cos\theta & -\sin\phi\sin\theta & \cos\phi \\ -\sin\theta & \cos\theta & 0 \\ -\cos\phi\cos\theta & -\cos\phi\sin\theta & -\sin\phi \end{bmatrix} \begin{bmatrix} 0 & \hat{z} & -\hat{y} \\ -\hat{z} & 0 & \hat{x} \\ \hat{y} & -\hat{x} & 0 \end{bmatrix} \begin{bmatrix} \Omega_{\hat{x}} \\ \Omega_{\hat{y}} \\ \Omega_{\hat{z}} \end{bmatrix}. \quad (2)$$

The rotational velocities are tangent to the Earth's surface and thus have no vertical component. However, in order to be complete, we describe the block model using a three component velocity vector.

The second term of the velocity field (equation 1) is the contribution from elastic strain accumulation due to the locking of faults during the interseismic part of the seismic cycle. In the limiting case that faults do not creep from the surface to an effective locking depth during the interseismic part of the seismic cycle, the rate of elastic strain accumulation is proportional to the long-term fault-slip rate (Savage and

Burford, 1973). This near surface interseismic locking produces a smooth velocity gradient from block to adjacent block across faults. This behavior has been observed across strike-slip faults globally, including the San Andreas (Savage and Burford, 1973), North Anatolian (Meade *et al.*, 2002), Dead Sea (Gomez *et al.*, 2007), and Kunlun (Hilley *et al.*, 2005) faults, as well as thrust faults such as those at the Himalayan Range Front (Bilham *et al.*, 1997). The interseismic elastic velocity field may be effectively represented by a coseismic slip deficit velocity resulting from either steady slip on a down-dip extension of the seismogenic fault (Savage and Burford, 1973) or as a result of a viscoelastic earthquake cycle in the limit that the earthquake repeat interval divided by the Maxwell time is less than unity. The elastic coseismic slip deficit velocity, $\tilde{\mathbf{v}}_{\mathrm{CSD}}$, due to a slip, $\mathbf{s}$, on a single fault is given by

$$\tilde{\mathbf{v}}_{\mathrm{CSD}} = \mathbf{P}_{\alpha}\mathbf{G}_{O}\mathbf{s} = \begin{bmatrix} \cos\alpha & -\sin\alpha & 0 \\ \sin\alpha & \cos\alpha & 0 \\ 0 & 0 & 1 \end{bmatrix} \begin{bmatrix} \partial\bar{v}_{\bar{x}}/\partial s_s & \partial\bar{v}_{\bar{x}}/\partial s_d & \partial\bar{v}_{\bar{x}}/\partial s_t \\ \partial\bar{v}_{\bar{y}}/\partial s_s & \partial\bar{v}_{\bar{y}}/\partial s_d & \partial\bar{v}_{\bar{y}}/\partial s_t \\ \partial\bar{v}_{\bar{z}}/\partial s_s & \partial\bar{v}_{\bar{z}}/\partial s_d & \partial\bar{v}_{\bar{z}}/\partial s_t \end{bmatrix} \begin{bmatrix} s_s \\ s_d \\ s_t \end{bmatrix} = \mathbf{G}_{\alpha O}\mathbf{s}, \tag{3}$$

where $\mathbf{G}_O$ gives the partial derivatives of the elastic Green's functions describing station response to slip, $\mathbf{s}$, on the fault (Okada, 1985), and s_s, s_d, and s_t are the strike-, dip-, and tensile-slip components of fault slip, respectively. The Green's functions describing surface displacements are linear functions of slip and Poisson's ratio but nonlinear functions of the fault dip, strike, and locking depth and are solutions to the Navier equations with a set of equivalent body forces at block boundaries. The strike, α, of a rectangular fault segment with endpoint coordinates $(\theta^{\{a\}}, \phi^{\{a\}})$ and $(\theta^{\{b\}}, \phi^{\{b\}})$ on a sphere is

$$\alpha = \tan^{-1}\left[\frac{\cos\phi^{\{a\}}\sin(\theta^{\{a\}} - \theta^{\{b\}})}{\cos\phi^{\{b\}}\sin\phi^{\{a\}} - \sin\phi^{\{b\}}\cos\phi^{\{a\}}\cos(\theta^{\{a\}} - \theta^{\{b\}})}\right], \tag{4}$$

so that $\mathbf{P}_{\alpha}$ rotates the velocity components to correct for the fault strike.

The elastic deformation rate is calculated on a planar surface in Cartesian space (Okada, 1985) requiring a projection to geographic coordinates. Traditionally, this problem has been addressed by selecting a single map projection for the study area of interest (e.g., Matsu'ura *et al.*, 1986; Feigl *et al.*, 1993; Hashimoto and Jackson, 1993; Bennett *et al.*, 1996). Conformal map projections preserve angles exactly and thus the relative azimuths of velocities. However, the areal distortion grows rapidly with the size of the study area. For a study area the size of California projected into planar Cartesian space using a Universal Transverse Mercator projection, the areal distortion reaches a maximum of ~2%, while using this same projection for an area spanning southern California to northern Alaska introduces an areal distortion of ~30%. Thus for large study areas a single map projection may introduce substantial errors in the relative distance between faults and GPS stations. This is a particularly important consideration due to the fact that the displacement field arising from slip on an infinitely long strike-slip dislocation falls off as $\sim r^{-1}$ at distances greater than one locking depth away from the fault trace. To avoid this source of spatial error we use optimal map projections for each fault segment. By optimal, we mean a map projection that is conformal yet produces minimal areal distortion in the vicinity of the fault where the elastic effects are most pronounced. For each fault segment, we use an oblique Mercator projection that is locally tangent to the fault trace and has a pole 90° from the segment midpoint. The pole location is given by the cross product of the Cartesian coordinates of the two fault segment endpoints (a, b) as, $\hat{\mathbf{p}}^{\mathrm{pole}} = \hat{\mathbf{p}}^{\{a\}} \times \hat{\mathbf{p}}^{\{b\}}$. Because this coordinate system is locally tangent to the surface of the sphere at the fault trace, the vertical displacements in planar Cartesian space, $\bar{v}_z(\bar{\mathbf{x}})$, give the up component of the velocity field in ENU space. However, because of the fact that the projection is oblique, the east and north velocities must be rotated by the angle α from planar Cartesian coordinates to the east and north velocity components. The rotation matrix $\mathbf{P}_{\alpha}$ exploits the choice of a conformal map projection and maps velocities from $\bar{x}$, $\bar{y}$ orientation to the east and north components through a rotation.

The kinematically consistent slip rate at the midpoint of a fault segment is proportional to the differential velocity predicted by the relative rotation of the bounding blocks (p and q in this case) on either side,

$$\mathbf{s} = \mathbf{P}_F\mathbf{P}_V\mathbf{G}_{\Delta\hat{\mathbf{v}}}\begin{bmatrix} \boldsymbol{\Omega}^{\{p\}} \\ \boldsymbol{\Omega}^{\{q\}} \end{bmatrix} = \mathbf{P}_F\mathbf{P}_V\begin{bmatrix} \mathbf{G}_B & -\mathbf{G}_B \end{bmatrix}\begin{bmatrix} \boldsymbol{\Omega}^{\{p\}} \\ \boldsymbol{\Omega}^{\{q\}} \end{bmatrix}, \tag{5}$$

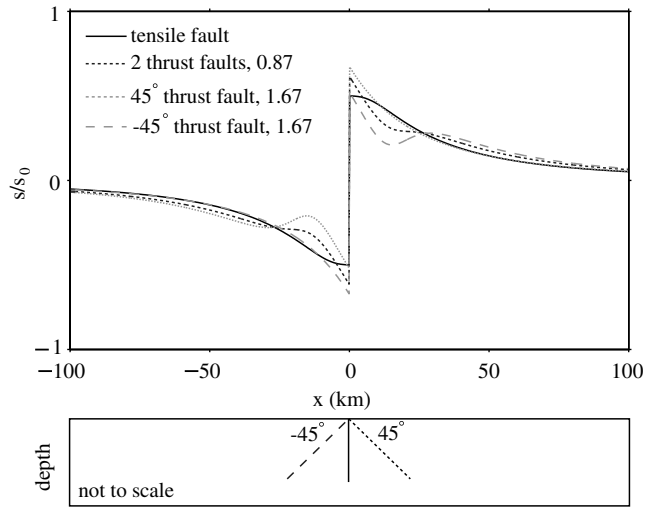

Figure 2. Horizontal deformation normal to the fault trace for vertical tensile and dipping reverse faults. The four profiles shown here are dip slip on a fault inclined 45° to the right (dashed gray line), dip slip on a fault inclined 45° to the left (dotted gray line), the combined effect of both the right- and left-dipping faults (dotted black line), and unit tensile slip on a vertical fault (black line). All faults are assumed locked to 15 km, and the lower panel shows an idealized representation of the model geometry at depth. The numbers following each profile label in the upper panel give the optimal slip rate for each of the cases calculated to best match the deformation predicted from the unit tensile-slip case. Note that for both the asymmetric cases (±45°) the best-fitting slip rate, 1.67, is greater than the resolved kinematically consistent slip rate, $\sqrt{2}$ (equation 6).

where the matrix $\mathbf{P}_F$ projects the differential east and north block motion velocity into fault-slip components and $\mathbf{G}_{\Delta\hat{\mathbf{v}}}$ gives the differential velocity at a fault segment midpoint due to the relative motion predicted by the rotation of the blocks that bound a fault to the east and west. The product $\mathbf{P}_V\mathbf{G}_{\Delta\hat{\mathbf{v}}}\boldsymbol{\Omega}$ gives the differential east and north components of velocity at the block boundary that can be rotated to obtain the fault parallel, $\Delta v_\parallel$, and fault perpendicular, $\Delta v_\perp$, slip rates using

$$\mathbf{P}_F = \begin{cases} \begin{bmatrix} \cos\alpha & -\sin\alpha & 0 \\ 0 & 0 & 0 \\ \sin\alpha & \cos\alpha & 0 \end{bmatrix} & \text{if } \delta = 90°, \\ \begin{bmatrix} \cos\alpha & -\sin\alpha & 0 \\ \sin\alpha/\cos\delta & \cos\alpha/\cos\delta & 0 \\ 0 & 0 & 0 \end{bmatrix} & \text{if } \delta \neq 90°, \end{cases} \tag{6}$$

where δ is the fault dip. For any given fault segment we allow only two slip components, strike slip and either dip or tensile slip. In all cases, $\Delta v_\parallel$ gives the strike-slip component of the slip vector, s_s. For vertical faults, $\Delta v_\perp$ describes opening or closing tensile motion across the fault, s_t, while for dipping faults, $\Delta v_\perp$ is the horizontal component of dip-slip motion, $s_d = \Delta v_\perp/\cos\delta$. This means that the dip-slip rate at depth will always be greater than the fault convergence rate but will be kinematically consistent with the horizontal block motions at the Earth's surface, where the constraining GPS measurements are made (Fig. 2).

Geodetic studies have demonstrated spatial variability in patterns of interseismic strain accumulation and its coseismic release (e.g., Harris and Segall, 1987; Bürgmann *et al.*, 2005), indicating that a uniform slip on a single rectangular fault plane may be insufficient to model the elastic deformation signal contained in the GPS data. To accurately model complex fault morphology and allow for spatially variable elastic coupling, we parameterize some fault surfaces using TDEs (e.g., Comninou, 1973; Brown, 1975; Jeyakumaran *et al.*, 1992; Thomas, 1993; Meade, 2007a). Note that along a fault segment with a TDE mesh, $\tilde{\mathbf{v}}_{\text{CSD}} = 0$, that is, there is no contribution to the elastic deformation field from a rectangular fault segment. Denoting the strike, dip, and tensile components of TDE slip as $\mathbf{t} = [t_s, t_d, t_t]^{\mathsf{T}}$, the elastic deformation contribution to the velocity field from an individual TDE can be written as

$$\tilde{\mathbf{v}}_{\text{TDE}} = \mathbf{P}_\alpha\mathbf{G}_T\mathbf{t} = \mathbf{G}_{\alpha T}\mathbf{t}, \tag{7}$$

where $\mathbf{G}_T$ is a matrix of partial derivatives of Green's functions describing displacements due to unit slip on a TDE (Comninou, 1973; Brown, 1975; Jeyakumaran *et al.*, 1992; Thomas, 1993; Meade, 2007a). As in the case of the rectangular fault segments, we project the triangular element and GPS station locations from spherical to Cartesian coordinates using a locally tangent oblique Mercator projection identical to the procedure described for the rectangular fault segments. The strike of a TDE, α, is defined as the azimuth of the great circle connecting two points lying at the same effective Earth radius (Fig. 3). We choose one of these points to be the intermediate-depth triangle vertex ($\mathbf{p}^{\{2\}}$) and then determine the coordinates of a second point along strike ($\mathbf{p}^{\{\text{as}\}}$) by solving for the intersection between a straight line segment and a sphere (e.g., Bourke, 1992):

$$\mathbf{p}^{\{\text{as}\}} = \mathbf{p}^{\{1\}} \pm f(\mathbf{p}^{\{3\}} - \mathbf{p}^{\{1\}}) \tag{8}$$

with $f = (-b \pm \sqrt{b^2 - 4ac})/2a$, where $a = ||\mathbf{p}^{\{3\}} - \mathbf{p}^{\{1\}}||^2$, $b = 2[\mathbf{p}^{\{1\}} \cdot (\mathbf{p}^{\{3\}} - \mathbf{p}^{\{1\}})]$, and $c = \|\mathbf{p}^{\{1\}}\|^2 - 2(\mathbf{p}^{\{1\}} \cdot \mathbf{p}^{\{3\}}) - R'^2$. The straight line segment in this case is that which connects the shallowest and deepest triangle vertices ($\mathbf{p}^{\{1\}}$ and $\mathbf{p}^{\{3\}}$), and the sphere is centered at the center of the Earth with radius equal to the effective Earth radius of the intermediate-depth vertex (R').

The nominally interseismic slip rates on a fault surface with spatially variable coupling are not necessarily kinematically consistent in the sense that they may differ from slip components predicted from differential block motion. Deviations from kinematically consistent (i.e., fully coupled) fault-slip rates require interpretation as either some sort of partial elastic coupling resulting from earthquake

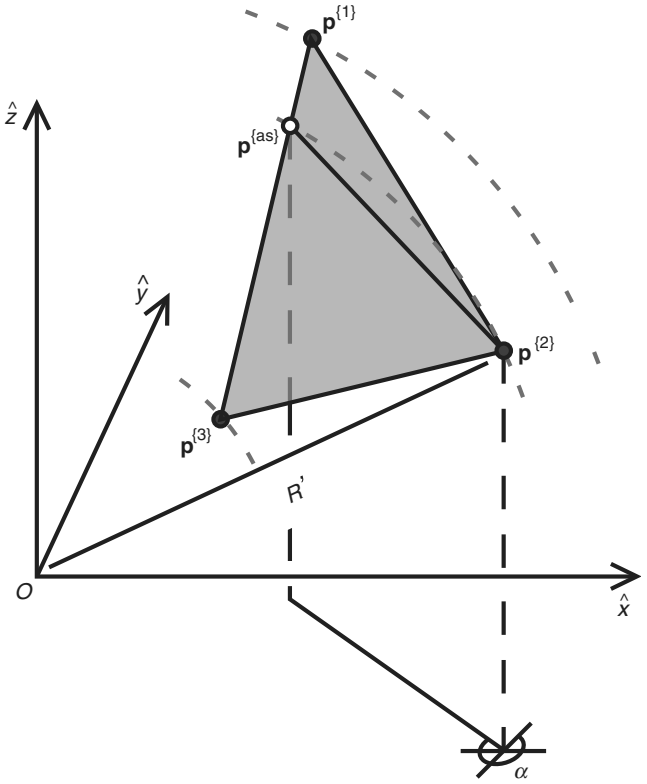

Figure 3. Schematic diagram showing the geometry of a single TDE, defined by its three vertices $\mathbf{p}^{\{i\}}$. The element strike, α, is determined by finding the azimuth of a horizontal line connecting the intermediate-depth vertex, $\mathbf{p}^{\{2\}}$, with a point, $\mathbf{p}^{\{as\}}$, lying at the same effective earth radius, R', along the side of the TDE opposite $\mathbf{p}^{\{2\}}$.

cycle processes (Meade and Loveless, 2009) or physical properties of the fault surface (e.g., Wallace *et al.*, 2007). In terms of the TDEs used here, the effective fault-slip rate can be written as a scaled version of the kinematically consistent fault-slip rate, $t_i = \chi_i t_i^{(k)}$, where χ_i is the so-called coupling coefficient typically ranging from zero to one, $t_i^{(k)}$ is the kinematically consistent slip rate, and the subscript i refers to the component of slip. This has been treated as a nonlinear problem where both χ_i and $t_i^{(k)}$ have been solved for simultaneously using either iterative or fully nonlinear estimation schemes (e.g., McCaffrey, 1995; Mazzotti *et al.*, 1999, 2000; McCaffrey, 2002; Nishimura *et al.*, 2007). However, fault slip that is not necessarily equal to that predicted by differential block motions may be estimated linearly by calculating $\mathbf{t}$ directly and then calculating the coupling coefficient *a posteriori* as $\chi_i = t_i / t_i^{(k)}$. Further, we do not constrain χ_i to lie in the range $0 \le \chi_i \le 1$ as this would preclude the detection of coseismic sense slip that characterizes documented earthquakes, slow slip events (e.g., Dragert *et al.*, 2001), and postseismic deformation (e.g., Nishimura *et al.*, 2004), all of which would be represented by negative χ_i values. The fully coupled and kinematically consistent fault-slip rate is recovered with $\chi_i = 1$.

Partially coupled faults appear pervasive in subduction zones, which, in many cases, have exceptionally large fault areas due to their shallow dips. This means that modeling subduction zones at the scales of interest often introduces such a large number of TDEs that the problem will become underdetermined. For example, tessellating the Nankai subduction zone at a mean length scale of 15 km requires 1868 TDEs, while the entire GeoNet GPS network in Japan has only 1224 GPS stations (Sagiya *et al.*, 2000). We regularize the inversion by imposing smoothing constraints on TDE slip vectors by solving for the slip distribution that simultaneously provides the best fit to the GPS data and simultaneously satisfies $\nabla^2 \mathbf{t} = 0$ (e.g., Harris and Segall, 1987; Maerten *et al.*, 2005). We express smoothing of the slip distribution around element i as

$$\mathbf{M}_T \mathbf{t}^{\{\xi\}} = \frac{2}{L^{\{\xi\}}} \sum_{j=1}^{n} \frac{\mathbf{t}^{\{j\}} - \mathbf{t}^{\{i\}}}{l^{\{ij\}}} = 0, \tag{9}$$

where the set of indices $\{\xi\}$ refers to the element i and its n neighboring elements, $\mathbf{t}^{\{i\}}$ is the slip on element i, $l^{\{ij\}}$ is the distance between the centroids of adjacent elements i and j, and $L^{\{\xi\}} = \sum_{j=1}^{n} l^{\{ij\}}$. Depending on the position of element i within the mesh of TDEs, n may equal 1, 2, or 3; elements within the mesh have 3 neighbors, those along the mesh perimeter may have 2 or 3, and those defining the mesh corners have 1 or 2. Each row of the linear smoothing operator, $\mathbf{M}_T$, will have 1, 2, or 3 off-diagonal nonzero entries depending on whether the corresponding element has 1, 2, or 3 neighbors, and the construction of the smoothing operator for the full triangular mesh is described in the Appendix. Additionally, *a priori* TDE slip rate constraints may be applied, $\mathbf{B}_T \mathbf{t} = \mathbf{t}_{bc}$, with the nonzero entries of sparse matrix $\mathbf{B}_T$ corresponding to those TDE slip components that are assumed. For example, this constraint may be used to apply up- or down-dip zero slip constraints on subduction zone interfaces (e.g., Flück *et al.*, 1997).

Thus far we have described velocity field contributions from block rotations and elastic strain accumulation on faults whose geometry we can explicitly represent. However, our knowledge of the deforming structures at plate boundary zones is incomplete and other distributed-deformation processes below the scale of model resolution may also contribute to the observed deformation field. In this case, intrablock deformation may represent faulting behavior at a scale smaller than that represented in a particular model and possibly additional deformation process. To account for these effects we follow McCaffrey (2005) and allow each of the blocks to deform as a result of uniform strain on a sphere (Love, 1906; Savage *et al.*, 2001). This rheology-free parametrization serves as a means for quantifying intrablock deformation and determining its percent contribution to the overall deformation budget. For each block, the contribution to the velocity field resulting from intrablock strain is

$$\tilde{\mathbf{v}}_{\dot{\epsilon}} = \mathbf{G}_{\dot{\epsilon}}\dot{\boldsymbol{\epsilon}} = \begin{bmatrix} R(\phi-\phi_0)\cos\theta_0 & R(\theta+\theta_0-\pi/2) & 0 \\ 0 & R(\phi-\phi_0)\cos\theta_0 & R(\theta+\theta_0-\pi/2) \\ 0 & 0 & 0 \end{bmatrix} \begin{bmatrix} \dot{\epsilon}_{\phi\phi} \\ \dot{\epsilon}_{\phi\theta} \\ \dot{\epsilon}_{\theta\theta} \end{bmatrix}, \tag{10}$$

where $\dot{\boldsymbol{\epsilon}}$ is the horizontal strain rate tensor and (ϕ_0, θ_0) define reference coordinates, where the magnitudes of the velocities due to strain are zero. McCaffrey (2005) assumed that (ϕ_0, θ_0) were located at the centroid of each block. While the block centroid does not necessarily represent the reference coordinates, locating these reference coordinates internal to each block ensures that the strain contributions for each block are linearly independent and minimizes the potential covariance of strain and rotation velocities. To illustrate this point, consider the idealized scenario where an Euler pole is located at the intersection of the equator and the Greenwich meridian. The northward velocity due to block rotation of a point located along the equator is $\tilde{v}_B = R\omega\sin\theta$, where θ is longitude (equal to the angular distance between the observation coordinates and the Euler pole), and ω is the rotation rate. From equation (10), the north component of the velocity field due to homogeneous strain interior to this block is $\tilde{v}_{\dot{\epsilon}} = R\dot{\epsilon}_{\phi\theta}(\theta-\theta_0)$. The north velocity components due to rotation and strain are similar where $\sin\theta \approx \theta - \theta_0$ (i.e., when the Euler pole is near θ_0, Savage *et al.*, 2001).

Summing the contributions from block rotations (equation 2) and internal block strain (equation 10), and subtracting the effect from elastic strain accumulation (equations 3 and 5–7), the nominally interseismic velocity $\tilde{\mathbf{v}}_I$ (equation 1) can be rewritten as the complete statement of the forward problem,

$$\begin{aligned} \tilde{\mathbf{v}}_I &= \tilde{\mathbf{v}}_B - (\tilde{\mathbf{v}}_{\mathrm{CSD}} + \tilde{\mathbf{v}}_{\mathrm{TDE}}) + \tilde{\mathbf{v}}_{\dot{\epsilon}} \\ &= \begin{bmatrix} (\mathbf{P}_V\mathbf{G}_B - \mathbf{G}_{\alpha O}\mathbf{P}_F\mathbf{P}_{V_2}\mathbf{P}_{\Delta\hat{\mathbf{v}}}) & -\mathbf{G}_{\alpha T} & \mathbf{G}_{\dot{\epsilon}} \end{bmatrix} \begin{bmatrix} \boldsymbol{\Omega} \\ \mathbf{t} \\ \dot{\boldsymbol{\epsilon}} \end{bmatrix}, \end{aligned} \tag{11}$$

which is a statement of the forward model for the simple case of one set of observation coordinates on a block moving with respect to a fixed exterior block. In general, we do not know the block motions, the spatial distribution of apparent elastic coupling, or internal strain rates, and instead seek to estimate these parameters given a set of present-day (≤20 yr) GPS velocities, $\underline{\tilde{\mathbf{v}}}_{\mathrm{GPS}}$, and geologically determined fault-slip rate constraints, $\underline{\mathbf{s}}_{\mathrm{obs}}$, while minimizing the gradient of the partially coupled slip distribution. Here we use the underbar notation to indicate the vectors and matrices generalized for an entire block model with multiple blocks, fault segments, GPS stations, etc., as shown in the Appendix. Additionally, boundary conditions such as no slip at the up- and/or down-dip limits of a subduction interface may be applied to the TDE slip distribution by specifying $\underline{\mathbf{t}}_{\mathrm{bc}}$. To solve for the best-fitting set of rotational block motions, $\underline{\boldsymbol{\Omega}}^{\mathrm{est}}$, TDE-slip rate vectors, $\underline{\mathbf{t}}^{\mathrm{est}}$, and internal block strain rate tensors, $\underline{\dot{\boldsymbol{\epsilon}}}^{\mathrm{est}}$, we generalize the linear combination (equation 11) for n_S GPS stations, n_B blocks, n_F fully coupled fault segments, and n_T TDEs, and use a weighted least-squares estimator:

$$\begin{bmatrix} \underline{\boldsymbol{\Omega}}^{\mathrm{est}} \\ \underline{\mathbf{t}}^{\mathrm{est}} \\ \underline{\dot{\boldsymbol{\epsilon}}}^{\mathrm{est}} \end{bmatrix} = (\underline{\mathbf{G}}^{\mathsf{T}}\underline{\mathbf{W}}\,\underline{\mathbf{G}})^{-1}\underline{\mathbf{G}}^{\mathsf{T}}\underline{\mathbf{W}} \begin{bmatrix} \underline{\tilde{\mathbf{v}}}_{\mathrm{GPS}} \\ \underline{\mathbf{s}}_{\mathrm{obs}} \\ 0 \\ \underline{\mathbf{t}}_{\mathrm{bc}} \end{bmatrix}, \tag{12}$$

where $\underline{\mathbf{W}}$ is the data, pseudodata, and boundary condition weighting matrix given by

$$\underline{\mathbf{W}} = \begin{bmatrix} \underline{\mathbf{C}}_{\mathrm{GPS}}^{-1} & 0 & 0 & 0 \\ 0 & \beta_1\underline{\mathbf{C}}_{\mathrm{obs}}^{-1} & 0 & 0 \\ 0 & 0 & \beta_2\mathbf{I} & 0 \\ 0 & 0 & 0 & \beta_3\underline{\mathbf{C}}_{\mathrm{bc}}^{-1} \end{bmatrix}, \tag{13}$$

where $\underline{\mathbf{C}}_{\mathrm{GPS}}$ is the GPS data covariance matrix, $\underline{\mathbf{C}}_{\mathrm{obs}}$ is the *a priori* slip rate covariance matrix, $\mathbf{I}$ is the identity matrix, $\underline{\mathbf{C}}_{\mathrm{bc}}$ is the TDE boundary condition covariance matrix, and β_i are the relative weights of the constraint data. The *a priori* slip rates are weighted by β_1, the strength of the smoothing constraint on the TDE-slip distribution is given by β_2, and the weights of the *a priori* slip rates on TDEs are given by β_3.

In equation (12), $\mathbf{G}$ is a combined generalized Jacobian given by

$$\underline{\mathbf{G}} = \begin{bmatrix} \underline{\mathbf{P}}_V\underline{\mathbf{G}}_B - \underline{\mathbf{G}}_{\alpha O}\underline{\mathbf{P}}_F\underline{\mathbf{P}}_{V_2}\underline{\mathbf{G}}_{\Delta\hat{\mathbf{v}}} & -\underline{\mathbf{G}}_{\alpha T} & \underline{\mathbf{G}}_{\dot{\epsilon}} \\ \underline{\mathbf{P}}_{F_2}\underline{\mathbf{P}}_{V_3}\underline{\mathbf{G}}_{\Delta\hat{\mathbf{v}}_2} & 0 & 0 \\ 0 & \underline{\mathbf{M}}_T & 0 \\ 0 & \underline{\mathbf{B}}_T & 0 \end{bmatrix}. \tag{14}$$

The matrices denoted with an underbar in $\underline{\mathbf{G}}$ are versions of the operators from equations (2), (5)–(7), and (10) generalized to multiple observation coordinates, blocks, fault segments, and TDEs (see the Appendix). Equation (12) can be solved directly for the case when the strain rate reference coordinates, and the weights, β_i, of the observations and pseudodata are assumed. Alternatively, the strain rate reference coordinates can be estimated efficiently by using a directed forward search that employs a penalty function to ensure that they lie within a particular block's boundaries. Only $\underline{\mathbf{G}}_{\dot{\epsilon}}$ needs to be modified for each set of reference coordinates; all other parameters can be estimated linearly, simultaneously minimizing the combined velocity field, *a priori* slip rates, and elastic coupling curvature residual. Processes such as postseismic relaxation due to either afterslip or viscoelastic relaxation of the lower crust/upper mantle may be superposed as additional deformation sources.

To illustrate how block theory enables the velocity field decomposition, we consider the GPS velocities in Japan from the GeoNet network (Sagiya *et al.*, 2000; see the Data and Resources section). The velocities in this field are averaged over the interval 1997–1999, and so they are not affected by macroscale seismicity but are influenced by both onshore faults and subduction zones (Hashimoto and Jackson, 1993; Le Pichon *et al.*, 1998). The observed velocity field is characterized by large trench-perpendicular velocities that generally decrease toward the northwest when viewed in a nominally Eurasian reference frame (Fig. 4a). Block models including the four major islands of Japan (Loveless and Meade, 2009) describe the observed velocity field to better than 1.76 mm/yr (Fig. 4b). Comparing contributions to the total velocity field from the estimated rotational (Fig. 4c) and elastic deformation fields (kinematically consistent, Fig. 4e; partially elastically coupled, Fig. 4f) shows how smoothly varying interseismic velocity fields can result from differencing component velocity vectors that differ in azimuth by ~180°. This is most clear on the island of Shikoku where the block component of the interseismic velocity field points toward the Nankai trough (Fig. 4c) and the velocities due to elastic strain accumulation point toward central Eurasia (Fig. 4f). Because the elastic component of the velocity field is larger than the block rotation component, the net interseismic motion on Shikoku is away from the trench but at a magnitude that is smaller than that of the elastic effect alone. This provides a clear example of the importance of understanding the relative contributions from each component of the velocity field. If block motion were neglected and all deformation on Shikoku were assumed to result entirely from elastic strain accumulation, then the rate of slip on the Nankai

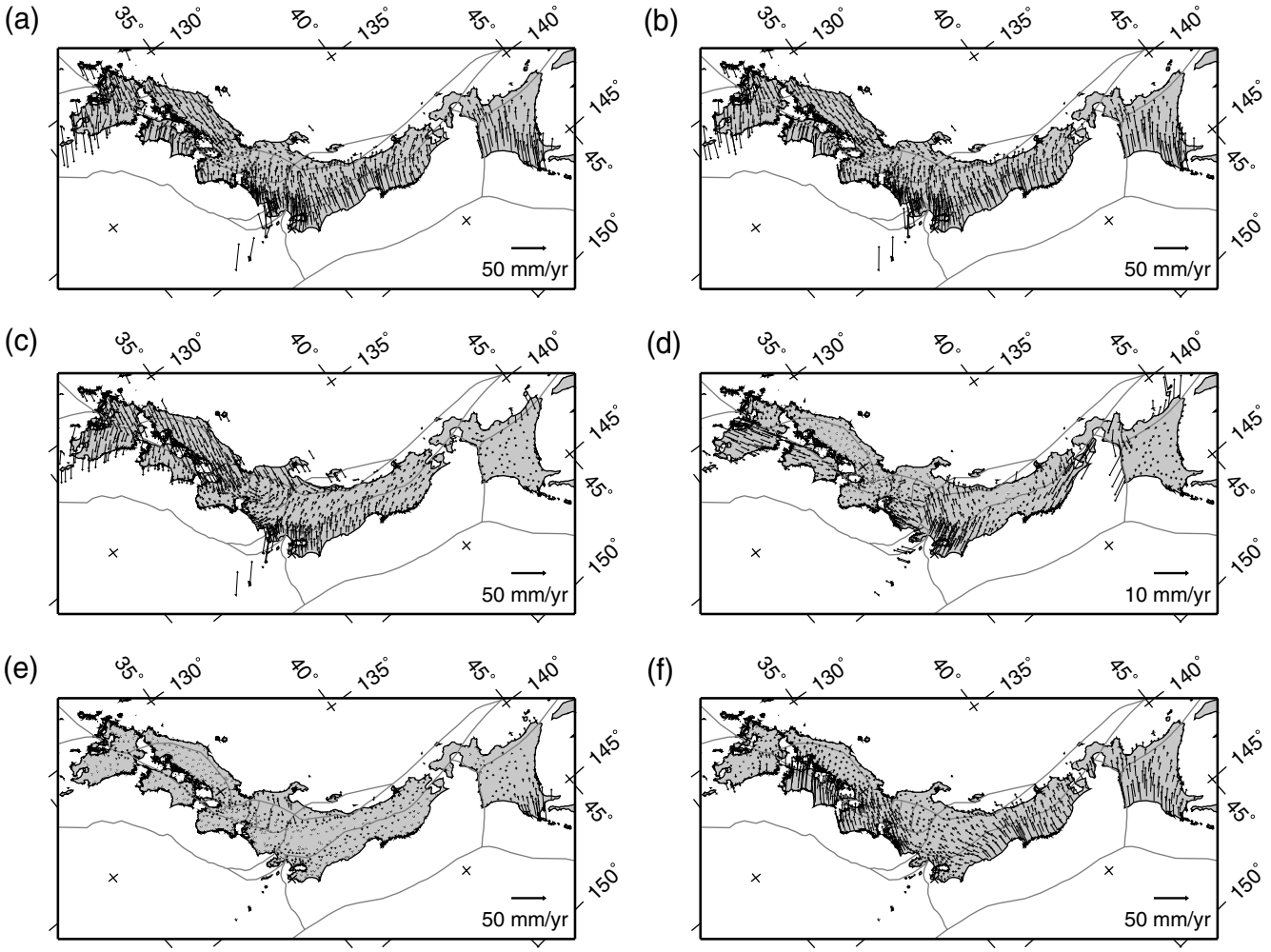

Figure 4. Velocity field decomposition from block model of Japan. Thin gray lines are the model block boundaries. (a) Observed GPS velocities in a nominal Eurasian reference frame. (b) Estimated model velocities from a block model equal to the sum of vectors in (c)–(f). (c) Velocities due to rotation of each block. (d) Velocities due to internal block strain. (e) Elastic velocities from fully coupled and kinematically consistent fault slip on rectangular dislocations at block boundaries. (f) Elastic velocities from TDE parametrization of variably coupled subduction zones. The large elastic velocities on the northeast tip of Hokkaido in (e) result from the transition from the portion of the fault tessellated by TDEs to that represented by a fully coupled rectangular fault segment. The cumulative contribution of both spatially variable coupling and the fully coupled rectangular subduction zone fault plane to the interseismic velocity field on Hokkaido can be seen in (b). The thick gray block model segments in (f) denote those that line the edge of a TDE mesh.

subduction zone would be underestimated. Note also that this block model allows us to see that the southeasterly velocities in Kyushu largely reflect the block motion, while the trench-perpendicular velocities in eastern Hokkaido have negligible contributions from both block rotation and internal block strain (Fig. 4d) and are instead dominated by elastic deformation. The effect of elastic deformation related to triangular elements and full-coupled fault segments is apparent in Figure 4e and f, where velocities measured at stations on the northeastern tip of Hokkaido, Japan, are largely influenced by the rectangular segment that lies beyond the extent of the subduction zone tessellated by TDEs, which contribute heavily to the velocities measured elsewhere on Hokkaido.

Fault-Network Connectivity and Segment Bounding Blocks

The methods described in the preceding section detail the construction and solution of a single block model. In practice it is often more useful to understand the behavior of multiple instances of block models with different fault-network geometries in order to select between models and quantify sensitivities. Fault-network geometries may differ (in terms of which faults are considered as block boundaries, fault azimuths, locking depths, the number of blocks, etc.) and such variations affect the fault-slip rate and block motion estimates. Most block model studies describe results from a single prescribed configuration of faults and blocks, while others present results from a preferred and small (<5) number of alternative models (e.g., d'Alessio *et al.*, 2005; Meade and Hager, 2005; McCaffrey *et al.*, 2007). Here we detail an unsupervised algorithm that determines the geometric parameters necessary to construct equation (12).

Testing different possible model geometries requires that the partial derivatives in equation (12) be calculated for each candidate block and fault geometry. The addition of a single fault segment can create a new block and thus change which blocks bound multiple fault segments including those that are not immediately adjacent to the added segment. While this is conceptually trivial, in practice it can prove to be a logistically challenging and time consuming bookkeeping exercise, especially so for models that include large numbers of faults and blocks. The practical challenges associated with the determination of the blocks that bound each fault segment (hereinafter referred to as block labels) has limited the study of multiple block model geometries in the past. Here we introduce an unsupervised algorithm that calculates the bounding block labels (e.g., p and q in equation 5) on the basis of the fault system geometry alone, without the need for *a priori* information about the total number of faults, blocks, or even how the fault segments are connected to one another.

The block closure and labeling algorithm requires that each fault segment is described by a surface trace with two endpoints, that no segment terminates at a location other than at the intersection with another segment, and that no segments strike exactly east–west or north–south. To begin with, each segment will have no block labels associated with it, that is, we have not yet determined which blocks bound the segments to the east and west. We solve this problem by extending previously hidden polygon algorithms for convex polygons (Franklin and Akman, 1986) to nonconvex polygons. The basic steps are to determine (1) which fault segments comprise a block, (2) the two unique labels of the blocks on either side of each fault segment, and (3) which of these two blocks are to the east and west of each segment. This algorithm is described conceptually here and graphically and in pseudocode in Figures 5 and 6, respectively. The algorithm proceeds to determine the total number of blocks and which segments bound each block by initially and arbitrarily picking a segment endpoint and then finding the other segments that connect to it at the opposite endpoint. If multiple segments are connected to the second endpoint then the leftmost of these along the look direction from the first to second endpoint is selected as the next segment in the block bounding polygon. For example, in Figure 5a, the fault segment $s^{\{1\}}$ intersects with segments $s^{\{2\}}$ and $s^{\{12\}}$ at its eastern termination (gray shaded region). Along the look direction (indicated by the arrow), the segment $s^{\{2\}}$ is the leftmost and will be selected as the next segment in the block. Similarly, at the eastern end of $s^{\{2\}}$, $s^{\{3\}}$ is the left-handed path and is thus chosen over $s^{\{7\}}$. The traverse starting from the western endpoint of fault segment $s^{\{1\}}$ proceeds in the sequence

$$s^{\{1\}} \rightarrow s^{\{2\}} \rightarrow s^{\{3\}} \rightarrow s^{\{4\}} \rightarrow s^{\{5\}} \rightarrow s^{\{6\}},$$

at which point the starting segment, $s^{\{1\}}$, is reached and the polygon defining a single block is complete. However, if the easternmost endpoint of s_1 were chosen first, then the look direction would be opposite to the direction shown in Figure 5a and the left-hand circulation rule determines the fault segments that define the exterior block,

$$s^{\{1\}} \rightarrow s^{\{6\}} \rightarrow s^{\{5\}} \rightarrow s^{\{4\}} \rightarrow s^{\{11\}} \rightarrow s^{\{10\}} \rightarrow s^{\{9\}} \rightarrow s^{\{8\}} \rightarrow s^{\{15\}} \rightarrow s^{\{14\}} \rightarrow s^{\{13\}} \rightarrow s^{\{12\}}$$

(block D in Figure 5b), enclosing each of the smaller blocks (A, B, and C). This left-hand rule ensures that the closure algorithm never traverses a block that contains another block unless it is the block that contains all other blocks, termed the exterior block (Fig. 6). After completing the traverse from all possible starting points, the number of uniquely defined polygons is equal to the total number of blocks. For each fault segment we can then determine which two blocks bound the segment by noting that a given fault segment can occur in no more than two different sets of polygon coordinates (Fig. 6). To identify the relative arrangement of the two bounding blocks, we make use of a test point (TP in Fig. 5a) that is placed 1 m due west of the midpoint longitude and latitude of a given segment. This places the test point within one of the two bounding blocks. For bounding

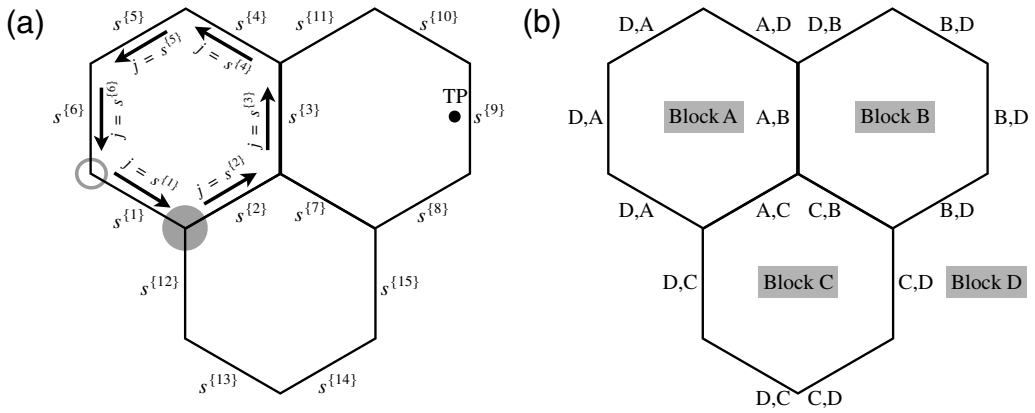

Figure 5. Geometry and results of block closure and labeling algorithm. The closure algorithm uses the endpoint coordinates of each fault segment to determine how many blocks there are and which blocks bound each fault segment to the east and west. (a) Geometry of the 15 fault segments and arrows indicating the direction of circulation starting from the western (leftmost) end point (hollow gray circle) of segment $s^{\{1\}}$. As the algorithm moves counterclockwise from the western to eastern endpoint of $s^{\{1\}}$, the leftmost branch at the triple junction (solid gray circle) is chosen, following segment $s^{\{2\}}$ rather than $s^{\{12\}}$. The block is considered closed when the original segment is returned to after traversing all segments j_F. The relative locations of the two bounding blocks (east and west) are determined for each fault segment by assessing whether or not a test point, TP, perturbed to the west of the segment midpoint, lies within the polygon. (b) The results of the block closure and labeling algorithm are shown here with A, B, C, and D as the labels for the four blocks (shaded), with block D termed the exterior block. Each segment is now associated with two labels separated by a comma, with the label of the western block to the left and the eastern block to the right.

blocks p and q (following equation 5), if the test point is within the polygon defined by all of the segments associated with block p, then block p lies to the west of the current fault segment. Alternatively, if the test point does not lie within the polygon defining block p, then it must lie within block q, and therefore block q lies to the west of the fault segment midpoint (Fig. 6). With the ordered vertices defining each block determined, it is trivial to assign a block label k to each station denoting the block on which it lies. This information is required to construct the generalized matrices in equation (14) (see the Appendix). This simple algorithm is a deterministic calculation and enables the efficient calculation of bounding block geometry and facilitates the modeling of multiple fault system geometries.

Discussion and Conclusions

GPS determined velocity fields provide decadal scale snapshots of the earthquake cycle behavior at plate boundary zones (e.g., GeoNet in Japan, Southern California Integrated GPS Network [SCIGN] in the United States). Here we describe a linear theory for block models to simultaneously estimate Euler poles, fault-slip rates, elastic coupling, and homogeneous intrablock strain in a spherical coordinate system. This theory provides a means for quantifying the roles played by both individual faults and crustal blocks to understand the internal consistency of proposed tectonic models. Additionally, block theory allows for the prediction of fault-slip rates and nominally interseismic velocities in regions where data are currently absent. These models have the potential to describe the majority of geodetically observed plate boundary zone deformation down to the ~1 mm/yr level (Meade, 2007b).

Understanding the implications of multiple tectonic models with different fault system geometries is necessary to precisely pose and answer questions about regional tectonics. To facilitate the analysis of alternative fault system geometries, we have developed an unsupervised block closure and labeling algorithm that determines the total number of blocks and which blocks lie to the east and west of each fault segment based solely on the geometry of the fault network. This algorithm allows for the efficient analysis of multiple fault-network geometries, so that fault slip uncertainties can be estimated not simply with respect to velocity field uncertainties, but also with respect to perturbations in fault system geometry including the effects of reducing or increasing the number of blocks. Construction of a block geometry is based on maps of active faults and seismicity. However, the spatial incompleteness of fault maps means that assembling a block geometry requires choices to be made in terms of which faults are considered and how each fault connects to others in the network. In addition to constraining fault-slip rates on previously recognized structures, block models may also help to identify faults whose tectonic significance was previously unknown, particularly in regions where active fault maps are incomplete.

Geodetic data now regularly provide spatially dense measurements of a nominally interseismic part of the seismic cycle. Block models are used to interpret these observations to estimate present-day fault-slip rates, block rotation rates, fault coupling, intrablock, and elastic strain accumulation rates. These quantities can be compared to both longer term deformation rates constrained by paleoseismological techniques, paleomagnetic observations, historical earthquake catalogs, and tectonic reconstructions as well as shorter term deformation reflected in coseismic slip distributions. These

$Q_F = n_F \times n_F$ matrix of zeros, temporary storage (n_F is number of segments)
$L_e = n_F \times 1$ matrix of zeros, east block label
$L_W = n_F \times 1$ matrix of zeros, west block label
for all segments (i_F) **do**
  Find segment j_F connected to segment i_F
  $n_j = 1$
  while $i_F \neq j_F$ **do**
    Add segment index j_F to block boundary segment list, $Q_F(i_F, n_j) = j_F$
    Find next connecting segment, j_F
    $n_j = n_j + 1$
  end while
end for
Identify unique blocks, Q_B as the n_B unique rows of Q_F
for all blocks (i_B) **do**
  for all non-zero elements of row i_B of Q_B, j **do**
    if $L_e(Q_B(j)) = 0$ **then**
      Assign current block label i_B as east label, $L_e(Q_B(j)) = i_B$
    else
      Assign current block label i_B as west label, $L_W(Q_B(j)) = i_B$
    end if
  end for
end for
for all segments (i_F) **do**
  if $L_e(i_F) = 0$ **then**
    Assign exterior block label as east label, $L_e(i_F) = n_B + 1$
  end if
  if $L_W(i_F) = 0$ **then**
    Assign exterior block label as west label, $L_W(i_F) = n_B + 1$
  end if
  Create test point, TP, west of segment i_F mid-point
  if TP not interior to block $L_W(i_F)$ **then**
    Swap east and west labels $L_e(i_F) \leftrightarrow L_W(i_F)$
  end if
end for

Figure 6. Pseudocode describing the block closure and labeling algorithm shown graphically in Figure 5.

comparisons have revealed varying degrees of agreement between geodetically and geologically determined fault-slip rates, including consistency along the Carrizo segment of the San Andreas fault (Sieh and Jahns, 1984; Meade and Hager, 2005) and apparent discrepancies in locales such as the strike-slip dominated eastern California shear zone (Oskin and Iriondo, 2004) and the largely extensional Basin and Range province (Friedrich *et al.*, 2003) of the western United States.

The model utilized in this article is based on an idealized concept of a two-phase earthquake cycle model consisting of coseismic and steady-state interseismic periods. The assumption of steady-state interseismic deformation is strictly justified only in the case of the relatively high viscosity lower crust/upper mantle and/or relatively long earthquake repeat intervals. In contrast, relatively low viscosity viscoelastic models have been successfully used to explain both short and long wavelength postseismic deformation (e.g., Pollitz *et al.*, 2000). These models make specific predictions as to the surface deformation rates throughout an entire earthquake cycle (Nur and Mavko, 1974; Savage and Prescott, 1978; Savage, 2000; Hetland and Hager, 2005, 2006) challenging the notion of a steady interseismic velocity field. The application of viscoelastic models to nominally interseismic velocity fields has remained somewhat limited and focused on the use of Maxwell rheologies for the lower crust/upper mantle (e.g., Savage and Lisowski, 1998; Pollitz *et al.*, 2008). The development of earthquake cycle models with generalized

linear (Hetland and Hager, 2005) and nonlinear rheologies may lead to the wider application of viscoelastic models due to the fact that deformation gradients may be localized near faults late in the earthquake cycle, consistent with geodetic observations prior to large earthquakes (e.g., McClusky *et al.*, 2000; Meade *et al.*, 2002). Viscoelastic models of earthquake cycle processes may also be combined with the block model framework to better understand tectonic motions, the layered rheology of the lithosphere, and perhaps, earthquake histories (e.g., Hetland and Hager, 2006).

Integrating instantaneous fault and block system activity through geologic time is an emerging challenge connecting earthquake cycle mechanics with the tectonic evolution of plate boundary zones. Dolan *et al.* (2007) have suggested coordinated changes in fault system activity between the Los Angeles basin and the eastern California shear zone through the Holocene, while Bennett *et al.* (2004) have considered how the southern San Andreas and San Jacinto faults may act in concert to accommodate Pacific–North American plate motions throughout the Quaternary. In these cases it has been argued that the acceleration of slip on one part of a fault system is accompanied by a corresponding deceleration on another so that the total slip budget is left unchanged. While the physical processes that control the development of plate boundary zones in geologic time are currently debated (e.g., Dolan *et al.*, 2007), block models provide a spatially coherent final condition against which temporal evolution models can be tested.

Data and Resources

The Global Positioning System data used in this study were collected by the Geographical Survey Institute of Japan and obtained from the Japan Association of Surveyors.

Acknowledgments

We thank Roland Bürgmann, an anonymous reviewer, and associate editor Fred Pollitz for thoughtful reviews. Jeff Freymueller's comments on an earlier draft led to substantial improvements. This research was supported by the Southern California Earthquake Center (SCEC). SCEC is funded by National Science Foundation (NSF) Cooperative Agreement EAR-0106924 and U.S. Geological Survey (USGS) Cooperative Agreement 02HQAG0008. The SCEC contribution number for this article is 1293.

References

Becker, T. W., J. L. Hardebeck, and G. Anderson (2005). Constraints on fault slip rates of the southern California plate boundary from GPS velocity and stress inversions, *Geophys. J. Int.* **160,** no. 2, 634–650.

Bennett, R., A. Friedrich, and K. Furlong (2004). Codependent histories of the San Andreas and San Jacinto fault zones from inversion of fault displacement rates, *Geology* **32,** no. 11, 961–964.

Bennett, R. A., W. Rodi, and R. E. Reilinger (1996). Global Positioning System constraints on fault slip rates in southern California and northern Baja, Mexico, *J. Geophys. Res.* **101,** no. B10, 21,943–21,960.

Bennett, R. A., B. P. Wernicke, J. L. Davis, P. Elosegui, J. K. Snow, M. J. Abolins, M. A. House, G. L. Stirewalt, and D. A. Ferrill (1997). Global Positioning System constraints on fault slip rates in the Death Valley region, California and Nevada, *Geophys. Res. Lett.* **24,** no. 23, 3073–3076.

Bilham, R., K. Larson, J. Freymueller, F. Jouanne, P. LeFort, P. Leturmy, J. L. Mugnier, J. F. Gamond, J. P. Glot, J. Martinod, N. L. Chaudury, G. R. Chitrakar, U. P. Gautam, B. P. Koirala, M. R. Pandey, R. Ranabhat, S. N. Sapkota, P. L. Shrestha, M. C. Thakuri, U. R. Timilsina, D. R. Tiwari, G. Vidal, C. Vigny, A. Galy, and B. deVoogd (1997). GPS measurements of present-day convergence across the Nepal Himalaya, *Nature* **386,** no. 6620, 61–64.

Bourke, P. (1992). Intersection of a line and a sphere (or circle), http://local.wasp.uwa.edu.au/pbourke/geometry/sphereline/ (last accessed September 2009).

Brown, R. L. (1975). A dislocation approach to plate interaction, *Ph.D. Thesis*, Massachusetts Institute of Technology.

Bürgmann, R., M. G. Kogan, G. M. Steblov, G. Hilley, V. E. Levin, and E. Apel (2005). Interseismic coupling and asperity distribution along the Kamchatka subduction zone, *J. Geophys. Res.* **110,** B07405, doi 10.1029/2005JB003648.

Comninou, M. (1973). Angular dislocation in a half space, *Ph.D. Thesis*, Northwestern University.

Cox, A., and R. Hart (1986). *Plate Tectonics: How it Works*, Blackwell Publishing, Oxford.

d'Alessio, M. A., I. A. Johanson, R. Burgmann, D. A. Schmidt, and M. H. Murray (2005). Slicing up the San Francisco Bay area: Block kinematics and fault slip rates from GPS-derived surface velocities, *J. Geophys. Res.-Solid Earth* **110,** no. B6, B06403, doi 10.1029/2004JB003496.

Dolan, J., D. Bowman, and C. Sammis (2007). Long-range and long-term fault interactions in southern California, *Geology* **35,** no. 9, 855–858, doi 10.1130/G23789A.1.

Dragert, H., K. Wang, and T. S. James (2001). A silent slip event on the deeper Cascadia subduction interface, *Science* **292,** no. 5521, 1525–1528.

England, P., and G. Houseman (1989). Extension during continental convergence, with application to the Tibetan plateau, *J. Geophys. Res.-Solid Earth Planets* **94,** no. B12, 17,561–17,579.

England, P., and D. McKenzie (1982). A thin viscous sheet model for continental deformation, *Geophys. J. R Astro. Soc.* **70,** no. 2, 295–321.

England, P., and P. Molnar (1997). Active deformation of Asia: From kinematics to dynamics, *Science* **278,** no. 5338, 647–650.

England, P., and P. Molnar (2005). Late Quaternary to decadal velocity fields in Asia, *J. Geophys. Res.* **110,** no. B12, B12401, doi 10.1029/2004JB003541.

England, P. C., and G. A. Houseman (1986). Finite strain calculations of continental deformation; 2, comparison with the India–Asia collision zone, *J. Geophys. Res.* **91,** no. B3, 3664–3676.

Feigl, K. L., D. C. Agnew, Y. Bock, D. Dong, A. Donnellan, B. H. Hager, T. A. Herring, D. D. Jackson, T. H. Jordan, R. W. King, S. Larsen, K. M. Larson, M. H. Murray, Z. K. Shen, and F. H. Webb (1993). Space geodetic measurement of crustal deformation in central and southern California, *J. Geophys. Res.* **98,** no. B12, 21,677–21,712.

Feldl, N., and R. Bilham (2006). Great Himalayan earthquakes and the Tibetan plateau, *Nature* **444,** 165–170.

Flesch, L. M., A. J. Haines, and W. E. Holt (2001). Dynamics of the India-Eurasia collision zone, *J. Geophys. Res.-Solid Earth* **106,** no. B8, 16,435–16,460.

Flesch, L. M., W. E. Holt, A. J. Haines, and B. M. Shen-Tu (2000). Dynamics of the Pacific–North American plate boundary in the western United States, *Science* **287,** no. 5454, 834–836.

Flück, P., R. D. Hyndman, and K. Wang (1997). Three-dimensional dislocation model for great earthquakes of the Cascadia subduction zone, *J. Geophys. Res.* **102,** no. B9, 20,539–20,550.

Franklin, W. R., and V. Akman (1986). Reconstructing visible regions from visible segments, *BIT* **26,** no. 4, 430–441.

Friedrich, A., B. Wernicke, N. Niemi, R. Bennett, and J. Davis (2003). Comparison of geodetic and geologic data from the Wasatch region,

Utah, and implications for the spectral character of Earth deformation at periods of 10 to 10 million years, *J. Geophys. Res.* **108,** no. B4, 2199, doi 10.1029/2001JB000682.

Genrich, J. F., Y. Bock, R. McCaffrey, L. Prawirodirdjo, C. W. Stevens, S. S. O. Puntodewo, C. Subarya, and S. Wdowinski (2000). Distribution of slip at the northern Sumatran fault system, *J. Geophys. Res.* **105,** no. B12, 28,327–28,341, doi 10.1029/2000JB900158.

Gomez, F., G. Karam, M. Khawlie, S. McClusky, P. Vernant, R. Reilinger, R. Jaafar, C. Tabet, K. Khair, and M. Barazangi (2007). Global Positioning System measurements of strain accumulation and slip transfer through the restraining bend along the Dead Sea fault system in Lebanon, *Geophys. J. Int.* **168,** no. 3, 1021–1028, doi 10.1111/j.1365-246X.2006.03328.x.

Haines, A. J., and W. E. Holt (1993). A procedure for obtaining the complete horizontal motions within zones of distributed deformation from the inversion of strain-rate data, *J. Geophys. Res.* **98,** no. B7, 12,057–12,082.

Harris, R., and P. Segall (1987). Detection of a locked zone at depth on the Parkfield, California, segment of the San Andreas fault, *J. Geophys. Res.* **92,** no. B8, 7945–7962.

Hashimoto, M., and D. D. Jackson (1993). Plate tectonics and crustal deformation around the Japanese islands, *J. Geophys. Rese.* **98,** no. B9, 16,149–16,166.

Hetland, E. A., and B. H. Hager (2004). Relationship of geodetic velocities to velocities in the mantle, *Geophys. Res. Lett.* **31,** L17604, doi 10.1029/2004GL020691.

Hetland, E. A., and B. H. Hager (2005). Postseismic and interseismic displacements near a strike-slip fault; a two-dimensional theory for general linear viscoelastic rheologies, *J. Geophys. Res.* **110,** B10401, doi 10.1029/2005JB003689.

Hetland, E. A., and B. H. Hager (2006). Interseismic strain accumulation; spin-up, cycle invariance, and irregular rupture sequences, *Geochem. Geophys. Geosys.* **7,** Q05004, doi 10.1029/2005GC001087.

Hilley, G. E., R. Burgmann, P. Z. Zhang, and P. Molnar (2005). Bayesian inference of plastosphere viscosities near the Kunlun fault, northern Tibet, *Geophys. Res. Lett.* **32,** no. 1, L01302, doi 10.1029/2004GL021658.

Holt, W. E., N. Chamot-Rooke, X. Le Pichon, A. J. Haines, B. Shen-Tu, and J. Ren (2000). Velocity field in Asia inferred from Quaternary fault slip rates and Global Positioning System observations, *J. Geophys. Res.* **105,** no. B8, 19,185–19,209.

Jeyakumaran, M., J. W. Rudnicki, and L. M. Keer (1992). Modeling slip zones with triangular dislocation elements, *Bull. Seismol. Soc. Am.* **82,** no. 5, 2153–2169.

Jouanne, F., J. L. Mugnier, J. F. Gamond, P. Le Fort, M. R. Pandey, L. Bollinger, M. Flouzat, and J. P. Avouac (2004). Current shortening across the Himalayas of Nepal, *Geophys. J. Int.* **157,** no. 1, 1–14.

Le Pichon, X., S. Mazzotti, P. Henry, and M. Hashimoto (1998). Deformation of the Japanese Islands and seismic coupling: An interpretation based on GSI permanent GPS observations, *Geophys. J. Int.* **134,** no. 2, 501–514.

Liu, Z., and P. Bird (2008). Kinematic modelling of neotectonics in the Persia-Tibet-Burma orogen, *Geophys. J. Int.* **172,** no. 2, 779–797.

Love, A. E. H. (1906). *A Treatise on the Mathematical Theory of Elasticity*, Second Ed., Cambridge University Press, Cambridge.

Loveless, J. P., and B. J. Meade (2009). Geodetic imaging of plate motions, fault slip rates, and partitioning of deformation in Japan, *J. Geophys. Res.* doi 10.1029/2008JB006248 (in press).

Maerten, F., P. Resor, D. D. Pollard, and L. Maerten (2005). Inverting for slip on three-dimensional fault surfaces using angular dislocations, *Bull. Seismol. Soc. Am.* **95,** no. 5, 1654–1665, doi 10.1785/0120030181.

Matsu'ura, M., D. D. Jackson, and A. Cheng (1986). Dislocation model for aseismic crustal deformation at Hollister, California, *J. Geophys. Res.* **91,** no. B12, 2661–2674.

Mazzotti, S., P. Henry, X. Le Pichon, and T. Sagiya (1999). Strain partitioning in the zone of transition from Nankai subduction to Izu-Bonin collision (central Japan): Implications for an extensional tear within the subducting slab, *Earth Planet. Sci. Lett.* **172,** no. 1–2, 1–10.

Mazzotti, S., X. Le Pichon, P. Henry, and S. Miyazaki (2000). Full interseismic locking of the Nankai and Japan-west Kurile subduction zones: An analysis of uniform elastic strain accumulation in Japan constrained by permanent GPS, *J. Geophys. Res.* **105,** no. B6, 13,159–13,177.

McCaffrey, R. (1995). DEFNODE Users' Guide, Rensselaer Polytechnical Institute, http://www.rpi.edu/$mccafr/defnode.

McCaffrey, R. (2002). Crustal block rotations and plate coupling, in *Plate Boundary Zones*, Geodynamics Series, **30**, S. Stein and J. T. Freymueller (Editors), 101–122, American Geophysical Union.

McCaffrey, R. (2005). Block kinematics of the Pacific-North America plate boundary in the southwestern United States from inversion of GPS, seismological, and geologic data, *J. Geophys. Res.* **110,** no. B7, B07401, doi 10.1029/2004JB003307.

McCaffrey, R., M. Long, C. Goldfinger, P. C. Zwick, J. L. Nabalek, C. K. Johnson, and C. Smith (2000). Rotation and plate locking at the southern Cascadia subduction zone, *Geophys. Res. Lett.* **27,** 3117–3120.

McCaffrey, R., A. Qamar, R. King, R. Wells, G. Khazaradze, C. Williams, C. Stevens, J. Vollick, and P. Zwick (2007). Fault locking, block rotation and crustal deformation in the Pacific Northwest, *Geophys. J. Int.* **169,** no. 3, 1315–1340, doi 10.1111/j.1365-246X.2007.03371.x.

McClusky, S., S. Balassanian, A. Barka, C. Demir, S. Ergintav, I. Georgiev, O. Gurkan, M. Hamburger, K. Hurst, H. Kahle, K. Kastens, G. Kekelidze, R. King, V. Kotzev, O. Lenk, S. Mahmoud, A. Mishin, M. Nadariya, A. Ouzounis, D. Paradissis, Y. Peter, M. Prilepin, R. Reilinger, I. Sanli, H. Seeger, A. Tealeb, M. N. Toksoz, and G. Veis (2000). Global Positioning System constraints on plate kinematics and dynamics in the eastern Mediterranean and Caucasus, *J. Geophys. Res.-Solid Earth* **105,** no. B3, 5695–5719.

Meade, B., and J. Loveless (2009). Predicting the geodetic signature of $M_w \geq 8$ slow slip events, *Geophys. Res. Lett.* **36,** no. 1, L01306.

Meade, B. J. (2007a). Algorithms for the calculation of exact displacements, strains, and stresses for triangular dislocation elements in a uniform elastic half space, *Comput. Geosci.* **33,** 1064–1075, doi 10.1016/j.cageo.2006.12.003.

Meade, B. J. (2007b). Power-law distribution of fault slip-rates in southern California, *Geophys. Res. Lett.* **34,** L23307, doi 10.1029/2007GL031454.

Meade, B. J., and B. H. Hager (2005). Block models of crustal motion in southern California constrained by GPS measurements, *J. Geophys. Res.* **110,** B03403, doi 10.1029/2004JB003209.

Meade, B. J., B. H. Hager, S. C. McClusky, R. E. Reilinger, S. Ergintav, O. Lenk, A. Barka, and H. Ozener (2002). Estimates of seismic potential in the Marmara Sea region from block models of secular deformation constrained by global positioning system measurements, *Bull. Seismol. Soc. Am.* **92,** no. 1, 208–215.

Minster, J. B., and T. H. Jordan (1987). Vector constraints on western United-States deformation from space geodesy, neotectonics, and plate motions, *J. Geophys. Res.* **92,** no. B6, 4798–4804.

Molnar, P. (1988). Continental tectonics in the aftermath of plate tectonics, *Nature* **335,** no. 6186, 131–137.

Molnar, P., and J. M. Gipson (1996). A bound on the rheology of continental lithosphere using very long baseline interferometry: The velocity of south China with respect to Eurasia, *J. Geophys. Res.* **101,** no. B1, 545–553.

Murray, M. H., and P. Segall (2001). Modeling broadscale deformation in northern California and Nevada from plate motions and elastic strain accumulation, *Geophys. Res. Lett.* **28,** no. 22, 4315–4318.

Nishimura, T., T. Hirasawa, S. Miyazaki, T. Sagiya, T. Tada, S. Miura, and K. Tanaka (2004). Temporal change of interplate coupling in northeastern Japan during 1995–2002 estimated from continuous GPS observations, *Geophys. J. Int.* **157,** no. 2, 901–916.

Nishimura, T., T. Sagiya, and R. S. Stein (2007). Crustal block kinematics and seismic potential of the northernmost Philippine Sea plate and

Izu microplate, central Japan, inferred from GPS and leveling data, *J. Geophys. Res.* **112,** B05414, doi 10.1029/2005JB004102.

Nur, A., and G. Mavko (1974). Postseismic viscoelastic rebound, *Science* **183,** no. 4121, 204–206.

Okada, Y. (1985). Surface deformation due to shear and tensile faults in a half-space, *Bull. Seismol. Soc. Am.* **75,** no. 4, 1135–1154.

Oskin, M., and A. Iriondo (2004). Large-magnitude transient strain accumulation on the Blackwater fault, Eastern California shear zone, *Geology* **32,** no. 4, 313–316.

Pollitz, F., P. McCrory, J. Svarc, and J. Murray (2008). Dislocation models of interseismic deformation in the western United States, *J. Geophys. Res.* **113,** B04413, doi 10.1029/2007JB005174.

Pollitz, F. F., G. Peltzer, and R. Burgmann (2000). Mobility of continental mantle: Evidence from postseismic geodetic observations following the 1992 Landers earthquake, *J. Geophys. Res.-Solid Earth* **105,** no. B4, 8035–8054.

Sagiya, T., S. Miyazaki, and T. Tada (2000). Continuous GPS array and present-day crustal deformation of Japan, *Pure Appl. Geophys.* **157,** no. 11–12, 2303–2322.

Savage, J. (2000). Viscoelastic-coupling model for the earthquake cycle driven from below, *J. Geophys. Res.* **105,** no. B11, 25,525–25,532.

Savage, J., and W. H. Prescott (1978). Asthenosphere readjustment and the earthquake cycle, *J. Geophys. Res.* **83,** no. B7, 3369–3376.

Savage, J. C. (1983). A dislocation model of strain accumulation and release at a subduction zone, *J. Geophys. Res.* **88,** no. B6, 4984–4996.

Savage, J. C., and R. O. Burford (1973). Geodetic determination of relative plate motion in central California, *J. Geophys. Res.* **78,** no. 5, 832–845.

Savage, J. C., and M. Lisowski (1998). Viscoelastic coupling model of the San Andreas fault along the big bend, southern California, *J. Geophys. Res.-Solid Earth* **103,** no. B4, 7281–7292.

Savage, J. C., W. J. Gan, and J. L. Svarc (2001). Strain accumulation and rotation in the eastern California shear zone, *J. Geophys. Res.* **106,** no. B10, 21,995–22,007.

Segall, P. (2002). Integrating geologic and geodetic estimates of slip rate on the San Andreas fault system, *Int. Geol. Rev.* **44,** no. 1, 62–82.

Shen, Z. K., J. N. Lü, M. Wang, and R. Bürgmann (2005). Contemporary crustal deformation around the southeast borderland of the Tibetan plateau, *J. Geophys. Res.* **110,** B11409, doi 10.1029/2004JB003421.

Shen-Tu, B. M., W. E. Holt, and A. J. Haines (1999). Deformation kinematics in the western United States determined from Quaternary fault slip rates and recent geodetic data, *J. Geophys. Res.* **104,** no. B12, 28,927–28,955.

Sieh, K. E., and R. H. Jahns (1984). Holocene activity of the San-Andreas fault at Wallace-Creek, California, *Geol. Soc. Am. Bull.* **95,** no. 8, 883–896.

Souter, B. J. (1998). Comparisons of geologic models to GPS observations in southern California, *Ph.D. Thesis*, Massachusetts Institute of Technology.

Thatcher, W. (2007). Microplate model for the present-day deformation of Tibet, *J. Geophys. Res.* **112,** B01401, doi 10.1029/2005JB004244.

Thomas, A. L. (1993). Poly3D: A three-dimensional, polygonal element, displacement discontinuity boundary element computer program with applications to fractures, faults, and cavities in the Earth's crust, *Master's Thesis*, Stanford University.

Wallace, L., J. Beavan, R. McCaffrey, K. Berryman, and P. Denys (2007). Balancing the plate motion budget in the South Island, New Zealand using GPS, geological and seismological data, *Geophys. J. Int.* **168,** no. 1, 332–352.

Wang, K., R. Wells, S. Mazzotti, R. D. Hyndman, and T. Sagiya (2003). A revised dislocation model of interseismic deformation of the Cascadia subduction zone, *J. Geophys. Res.* **108,** no. B1, 2026, doi 10.1029/2001JB001227.

Zatman, S. (2000). On steady rate coupling between an elastic upper crust and a viscous interior, *Geophys. Res. Lett.* **27,** no. 16, 2421–2424.

Appendix

Assembly of Generalized Matrices

The matrices with underbars in equation (14) are generalized versions of the corresponding matrices in the main text replicated to the appropriate number of rows and columns necessary to accommodate the fault and block system geometry, *a priori* constraints, smoothing constraints, and GPS velocities. Here we show how each of these matrices can be assembled from their constituent parts. Parameters inside curly braces refer to a specific element of a vector or matrix while those inside parentheses indicate that a matrix or vector is a function of the given parameters. In each case the counting variables i and j should be iterated over all possible values. The subscripts S, F, B, and T indicate GPS stations (n_S total), faults (n_F total), blocks (n_B total), and TDEs (n_T total), respectively. For the subsequent matrices, we construct each from the basic 3×3 matrices and let each of the counting variables index into each 3×3 block of the generalized matrices. Throughout, $N_* = 3n_*$.

Starting with the top row of equation (14), the generalized matrix of partial derivatives for each GPS station with respect to the Cartesian rotation vector for the block on which it lies is given by a sparse $N_S \times N_B$ matrix, $\mathbf{G}_B$, with nonzero entries at

$$\underline{\mathbf{G}}_B\{i_S, k\{i_S\}\} = \mathbf{G}_B(i_S), \tag{A1}$$

where k is a vector of block labels for all stations, and the terms in curly brackets give submatrix indices into which the appropriate $\mathbf{G}_B$ should be placed for each GPS station, i_S. $\mathbf{G}_B$ is a function of the i_S element of the generalized station coordinate array including, for example, Cartesian vectors containing station location, $\underline{\hat{x}}$, $\underline{\hat{y}}$, and $\underline{\hat{z}}$.

The generalized matrix $\underline{\mathbf{P}}_V$ converting the XYZ rotation velocities to ENU velocities is block diagonal,

$$\underline{\mathbf{P}}_V\{i_S, i_S\} = \mathbf{P}_V(i_S), \tag{A2}$$

where $\mathbf{P}_V$ is a function of the i_S element of the generalized Cartesian vectors containing all station coordinates, $\hat{x}$, $\hat{y}$, and $\hat{z}$.

The generalized matrix, $\underline{\mathbf{G}}_{\Delta\hat{\mathbf{v}}}$ ($N_F \times N_B$), containing the partial derivatives of the differential Cartesian velocities at fault midpoints is nonzero at

$$\underline{\mathbf{G}}_{\Delta\hat{\mathbf{v}}}\{i_F, p\{i_F\}\} = \mathbf{G}_B(i_F) \tag{A3}$$

and

$$\underline{\mathbf{G}}_{\Delta\hat{\mathbf{v}}}\{i_F, q\{i_F\}\} = -\mathbf{G}_B(i_F), \tag{A4}$$

where the east and west block label vectors p and q are determined by the block closure and labeling algorithm described in the main text. Similarly, for the n_{ap} *a priori* fault-slip rate constraints $\underline{\mathbf{G}}_{\Delta\hat{\mathbf{v}}_2}$ is an $N_B \times 3n_{\text{ap}}$ matrix.

Table A1

List of Symbols Used in This Article

Symbol	Matrix Size	Description
	Geometric Parameters	
$\hat{\mathbf{x}} = [\hat{x}, \hat{y}, \hat{z}]$	$3n_S$	Cartesian
$\tilde{\mathbf{x}} = [\theta, \phi, R]$	$3n_S$	spherical
$\bar{\mathbf{x}}$	$3n_S$	planar
α	n_F or n_T	fault strike
δ	n_F or n_T	fault dip
$\{i\}$	1	(superscripted) index of geometric entity
θ_0, ϕ_0	$n_{\mathbf{B}}$	strain reference coordinates
$l^{\{ij\}}$	1	distance between centroids of elements i and j
	Velocity Vectors	
$\hat{\mathbf{v}}_*$	$3n_S$	Cartesian
$\tilde{\mathbf{v}}_*$	$3n_S$	spherical
$\bar{\mathbf{v}}_*$	$3n_S$	planar
$\mathbf{v}_I$	$3n_S$	interseismic
$\mathbf{v}_B$	$3n_S$	block rotation
$\mathbf{v}_E$	$3n_S$	total elastic strain accumulation
$\mathbf{v}_{\dot{\epsilon}}$	$3n_S$	intrablock strain rate
$\mathbf{v}_{\text{CSD}}$	$3n_S$	coseismic slip deficit
$\mathbf{v}_{\text{TDE}}$	$3n_S$	TDE
	Known Quantities	
$\underline{\mathbf{v}}_{\text{GPS}}$	$3n_S$	set of GPS velocities
$\underline{\mathbf{s}}_{\text{obs}}$	n_{ap}	*a priori* fault-slip rates
0	$3n_T$	curvature minimization (smoothing) vector
$\underline{\mathbf{t}}_{\text{bc}}$	n_{bc}	triangular element boundary conditions
$\underline{\mathbf{C}}_{\text{GPS}}$	$3n_S \times 3n_S$	GPS data covariance matrix
$\underline{\mathbf{C}}_{\text{obs}}$	$n_{\text{ap}} \times n_{\text{ap}}$	*a priori* slip rate covariance matrix
$\underline{\mathbf{C}}_{\text{bc}}$	$n_{\text{bc}} \times n_{\text{bc}}$	triangular boundary condition covariance matrix
	Constants	
β_1	1	*a priori* slip rate weighting
β_2	1	TDE slip smoothing weighting
β_3	1	TDE boundary condition weighting
R	1	Earth's radius
R'	1	effective Earth radius
	Solution Vectors	
$\boldsymbol{\Omega}$	$3n_B$	Cartesian rotation
$\mathbf{t}$	$3n_T$	TDE slip
$\dot{\boldsymbol{\epsilon}}$	$3n_B$	intrablock strain rate tensor component
$\mathbf{s}$	$3n_F$	rectangular segment slip vector
	Linear Operators—Each Submatrix is 3×3	
$\underline{\mathbf{P}}_V$	$3n_S \times 3n_S$	Cartesian to ENU conversion
$\underline{\mathbf{P}}_{V_2}$	$3n_F \times 3n_F$	Cartesian to ENU conversion
$\underline{\mathbf{P}}_F$	$3n_F \times 3n_F$	east, north to strike- and dip-slip conversion
$\underline{\mathbf{P}}_{F_2}$	$n_{\text{ap}} \times 3n_F$	east, north to strike- and dip-slip conversion
$\underline{\mathbf{P}}_{\Delta v}$	$3n_F \times 3n_B$	differential block motion to fault slip projection
$\underline{\mathbf{G}}_B$	$3n_S \times 3n_B$	cross product
$\underline{\mathbf{G}}_{\alpha O}$	$3n_S \times 3n_F$	rectangular dislocation element Green's functions
$\underline{\mathbf{G}}_{\alpha T}$	$3n_S \times 3n_T$	TDE Green's functions
$\underline{\mathbf{G}}_{\dot{\epsilon}}$	$3n_S \times 3n_B$	strain rate tensor components
$\underline{\mathbf{M}}_T$	$3n_F \times 3n_F$	TDE slip distribution smoothing
$\underline{\mathbf{B}}_T$	$n_{\text{bc}} \times 3n_T$	TDE boundary conditions identity matrix

The * subscript denotes a wildcard, applicable to any variable of the noted form. The matrix sizes are given as multiples of the number of variables used in the model: n_S is the number of GPS stations, n_F is the number of rectangular fault segments, n_T is the number of TDEs, n_B is te number of blocks, n_{ap} is the number of *a priori* fault-slip rate constraints, and n_{bc} is the number of TDE slip rate constraints.

The differential Cartesian velocities are rotated to an ENU coordinate system by an $N_F \times N_F$ block diagonal matrix,

$$\underline{\mathbf{P}}_{V_2}\{i_F, i_F\} = \mathbf{P}_V(i_F), \tag{A5}$$

and these differential velocities are projected onto the fault geometry by an $N_F \times N_F$ block diagonal matrix,

$$\underline{\mathbf{P}}_F\{i_F, i_F\} = \mathbf{P}_F(i_F), \tag{A6}$$

to give the two components of fault slip, $\Delta v_\parallel$ and $\Delta v_\perp$. Similarly, for the n_{ap} *a priori* fault-slip rate constraints $\underline{\mathbf{P}}_{V_3}$ is a $3n_{\text{ap}} \times 3n_{\text{ap}}$ matrix. $\underline{\mathbf{P}}_{F_2}$ is constructed initially as a $3n_F \times 3n_F$ with submatrices $\underline{\mathbf{P}}_F$, then reduced to a $3n_{\text{ap}} \times 3n_{\text{ap}}$ matrix by maintaining only the rows associated with the n_{ap} *a priori* slip rate constraints.

The partial derivatives for the kinematically consistent fault-slip rates on rectangular fault segments are given by the dense matrix $\underline{\mathbf{G}}_O$ composed of $N_S \times N_F$ submatrices, modified by the fault azimuth α,

$$\underline{\mathbf{G}}_{\alpha O}\{i_S, j_F\} = \mathbf{G}_{\alpha O}(i_S, j_F). \tag{A7}$$

Similarly, the partial derivative matrices used to calculate the contribution from the TDEs to the observed velocity field comprise the $N_S \times N_T$ generalized matrix modified by the azimuths of the elements:

$$\underline{\mathbf{G}}_{\alpha T}\{i_S, j_T\} = \mathbf{G}_{\alpha T}(i_S, j_T). \tag{A8}$$

The last contribution to the velocity field is from the internal block strain rates, $\underline{\mathbf{G}}_{\dot{\epsilon}}$ $(N_S \times N_B)$, given by

$$\underline{\mathbf{G}}_{\dot{\epsilon}}\{i_S, j_B\} = \mathbf{G}_{\dot{\epsilon}}(i_S, j_B). \tag{A9}$$

A set of n_{ap} *a priori* (typically geological) constraints on fault-slip rates are given in the second row of equation (14). The differential Cartesian velocities at each fault midpoint with an *a priori* fault-slip rate constraint are $\underline{\mathbf{P}}_{\Delta\hat{\mathbf{v}}_2}\{i_F, p_{\text{ap}}\{i_F\}\} = \mathbf{G}_B(i_F)$ and $\underline{\mathbf{P}}_{\Delta\hat{\mathbf{v}}_2}\{i_F, q_{\text{ap}}\{i_F\}\} = -\mathbf{G}_B(i_F)$, where p_{ap} and q_{ap} are vectors containing the east and west block labels for each of the fault segments with an *a priori* fault-slip rate constraint. These labels are determined by the same block closure and labeling algorithm as is used to determine p and q. The differential velocities are converted to strike-slip and dip- or tensile-slip components by $\underline{\mathbf{P}}_{F_2}\{i_F, i_F\} = \mathbf{P}_F(i_F)$.

We express smoothing of the slip distribution around element i as

$$\mathbf{M}_T\mathbf{t}^{\{\xi\}} = \frac{2}{L^{\{\xi\}}}\sum_{j=1}^{n}\frac{\mathbf{t}^{\{j\}} - \mathbf{t}^{\{i\}}}{l^{\{ij\}}} = 0, \tag{A10}$$

where the set of indices $\{\xi\}$ refers to the element i and its n neighboring elements.

Expanding (A10) for the case when $n = 3$ (i.e., element i does not lie on the edge of the mesh) gives

$$\left(\frac{2}{l^{\{i1\}} + l^{\{i2\}} + l^{\{i3\}}}\right)\left(\frac{\mathbf{t}^{\{1\}} - \mathbf{t}^{\{i\}}}{l^{\{i1\}}} + \frac{\mathbf{t}^{\{2\}} - \mathbf{t}^{\{i\}}}{l^{\{i2\}}} + \frac{\mathbf{t}^{\{3\}} - \mathbf{t}^{\{i\}}}{l^{\{i3\}}}\right) = 0,$$

$$\left(\frac{2}{l^{\{i1\}} + l^{\{i2\}} + l^{\{i3\}}}\right)\left(-\mathbf{t}^{\{i\}}\left(\frac{1}{l^{\{i1\}}} + \frac{1}{l^{\{i2\}}} + \frac{1}{l^{\{i3\}}}\right) + \frac{\mathbf{t}^{\{1\}}}{l^{\{i1\}}} + \frac{\mathbf{t}^{\{2\}}}{l^{\{i2\}}} + \frac{\mathbf{t}^{\{3\}}}{l^{\{i3\}}}\right) = 0,$$

and expressing as a linear operator gives

$$\gamma\begin{bmatrix} -f & d_1 & d_2 & d_3 \end{bmatrix}\begin{bmatrix} \mathbf{t}^{\{i\}} \\ \mathbf{t}^{\{1\}} \\ \mathbf{t}^{\{2\}} \\ \mathbf{t}^{\{3\}} \end{bmatrix} = 0,$$

$$\gamma\mathbf{m}_T\mathbf{t}^{\{\xi\}} = 0, \qquad \mathbf{M}_T\mathbf{t}^{\{\xi\}} = 0, \tag{A11}$$

where $\gamma = 2/L^{\{\xi\}}$, $d_j = 1/l^{\{ij\}}$, and $f = \sum_{j=1}^{n} 1/l^{\{ij\}}$. When the generalized linear smoothing operator, $\underline{\mathbf{M}}_T$, is constructed for the entire mesh of n_T TDEs, $\underline{\mathbf{M}}_T$ is a square, $3n_T \times 3n_T$ sparse matrix with each row serving to smooth one component of the element slip vector, $\mathbf{t}^{\{i\}}$. Entries $-\gamma f$ lie on the main diagonal, and the off-diagonal elements (of form γd_j) of each row multiply the appropriate slip component of the adjacent elements, $\mathbf{t}^{\{j\}}$. The generalized matrix, $\underline{\mathbf{B}}_T$, corresponding to n_{bc} TDE boundary conditions is an $n_{\text{bc}} \times 3n_T$ sparse matrix.

Department of Earth and Planetary Sciences
Harvard University
20 Oxford Street
Cambridge, Massachusetts 02138
meade@fas.harvard.edu

Manuscript received 3 April 2009